Aerodynamic Effects of Gurney Flaps on the Rotor Blades of a Research Wind Turbine

Jörg Alber[1], Rodrigo Soto-Valle[1], Marinos Manolesos[2], Sirko Bartholomay[1], Christian Navid Nayeri[1], Marvin Schönlau[1], Christian Menzel[1], Christian Oliver Paschereit[1], Joachim Twele[3], Jens Fortmann[3]

[1] Technische Universität Berlin, Hermann-Föttinger Institut, Müller-Breslau-Str. 8, 10623 Berlin, Germany
[2] College of Engineering, Swansea University, Bay Campus, Fabian Way, Swansea, SA1 8EN, United Kingdom
[3] Hochschule für Technik und Wirtschaft Berlin, Wilhelminenhofstraße 75A, 12459 Berlin, Germany

Correspondence to: Jörg Alber (joerg.alber@htw-berlin.de)

Abstract.

This paper investigates the aerodynamic impact of Gurney flaps on a research wind turbine of the Hermann-Föttinger Institute at the Technische Universität Berlin. The rotor radius is 1.5 meters and the blade configurations consist of the clean and the tripped baseline cases emulating the effects of forced leading edge transition. The wind tunnel experiments include three operation points based on tip speed ratios of 3.0, 4.3 and 5.6, reaching Reynold numbers of approximately $2.5 \cdot 10^5$. The measurements are taken by means of three different methods; Ultrasonic Anemometry in the wake, surface pressure taps in the mid-span blade region and strain gauges at the blade root. The retrofit applications consist of two Gurney flap heights of 0.5 % and 1.0 % in relation to the chord length, which are implemented perpendicular to the pressure side at the trailing edge. As a result, the Gurney flap configurations lead to performance improvements in terms of the axial wake velocities, the angles-of-attack and the lift coefficients. The enhancement of the root bending moments imply an increase of both the rotor torque and the thrust. Furthermore, the aerodynamic impact appears to be more pronounced in the tripped case compared to the clean case. Gurney flaps are considered a passive flow-control device worth investigating for the use on horizontal axis wind turbines.

1 Introduction

The energy yield of modern Horizontal Axis Wind Turbines (HAWTs) is supposed to be optimal while keeping the maintenance costs as low as possible over a lifetime of around 20 years. However, the performance of rotor blades faces serious challenges, two of which are early separation and roughness effects. Early separation is a problem especially in the inner blade region towards the root where the Angles-of-attack (AoA) are elevated due to structural constraints, such as limited chord-length and twist-angles, see Figure 1 (a). Over time, the resulting dynamic loads contribute to the material fatigue of the blade (Mueller-Vahl et al., 2012). For this reason, Passive Flow Control (PFC) devices, such as Vortex Generators (VGs), are implemented in the inner blade region of different-size HAWTs aiming at stall delay (Pechlivanoglou et. al., 2013). At the same time, the longstanding surface erosion causes roughness effects, especially close to the Leading Edge (LE), see Figure 1 (b). LE roughness is relevant throughout the entire blade span and especially in the outer region towards the blade tip. Apart from the broad range of weather conditions, surface roughening is aggravated by rain, insects as well as sand or salt particles. Consequently, the energy yield of HAWTs is often found lower than predicted or regressing over time (Wilcox et al., 2017).

(a) (b)

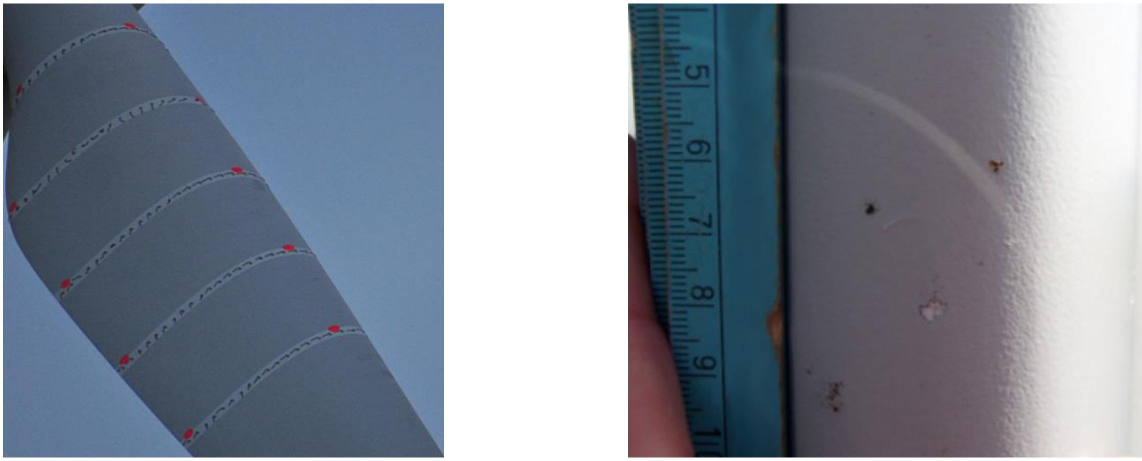

Figure 1. Rotor blades of utility scale wind turbines (a) Flow indicators to detect early separation in the inner blade region, reproduced from Pechlivanoglou et al. (2013). (b) Leading edge roughness, reproduced from Pechlivanoglou et al. (2010).

This paper investigates the retrofit application of Gurney Flaps (GFs) in order to improve the aerodynamic performance of rotor blades. This PFC device consists of a wedge- or right-angle profile that is attached perpendicular to the pressure side at the Trailing Edge (TE). The GF-height, *GF*, in relation to the chord-length is the main design parameter, illustrated in Figure 2 (a). It is usually in the range of 0.5 %c < *GF* < 2.0 %c without taking the TE thickness into account.

(a) (b)

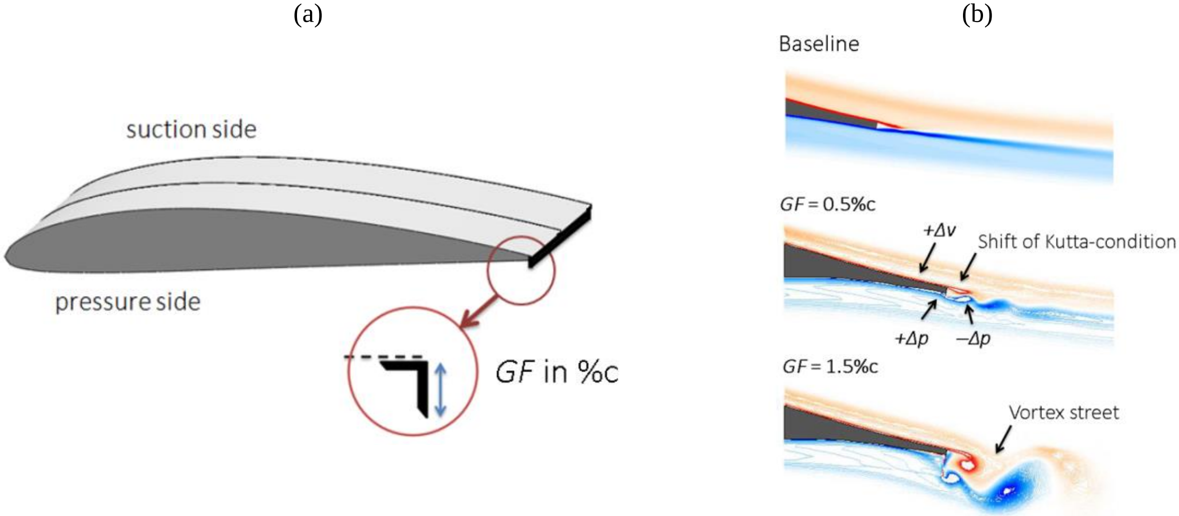

Figure 2. (a) Position of the Gurney flap at the trailing edge of a Clark-Y airfoil section. (b) CFD simulation of the HQ17 airfoil at $Re = 1.0 \cdot 10^6$, reproduced and modified from Schatz et al. (2004).

The research on TE flaps of airplane wings dates back to the early 20th century (Gruschwitz and Schrenk, 1933). The GF itself is named after the racecar driver Dan Gurney who discovered the significant gain in downforce when applying the device on the rear spoilers. Following from that, GFs have been implemented on high-lift dependent transport airliners (Bechert et al., 2000) and helicopter stabilizers (Houghton, 2013). More recently, Vestas® has started offering GFs in combination with VGs as so-called aerodynamic upgrades of HAWTs, predicting annual yield improvements of up to 2 % (Vestas, 2020). The design of the DTU 10 MW Reference turbine includes smooth wedge-shaped GFs in the first half of the blade length, 0.05R < r < 0.4R using GF-heights in the range of 3.5 %c < GF < 1.3 %c (Bak et al., 2013).

Figure 2 (b) illustrates the changes in the flow field of the laminar airfoil HQ17 when implementing different GF-heights, as reported by Liebeck (1978) by means of the Newman airfoil. Key to the aerodynamic understanding is the development of one vortex upstream and two counter-rotating vortices downstream of the GF, as such entailing a low-pressure region in the TE wake. As a result, the downwash angle of the flow becomes steeper, the requirements for pressure recovery on the suction side milder, the local boundary layer thinner and the suction peak higher. Additionally, the flow on the pressure side decelerates leading to a positive pressure built-up in the TE region. The resulting shift of the Kutta-condition leads to increased circulation and thus to elevated lift forces, which is the main Gurney flap characteristic. At the same time, the low-pressure region aft the TE induces additional drag, especially if vortex shedding is initiated in the form of a Kármán vortex street. Hence, the lift increase is accompanied by a certain drag penalty that affects the Lift-to-Drag (L/D) ratio accordingly.

That is why various experimental and numerical research projects aim at limiting the adverse drag increase while maintaining the beneficial lift enhancement of GFs. Giguère et al. (1995) and Kentfield (1996) conclude that the GF-height is supposed to be submerged into the local Boundary Layer (BL) in order to keep the drag on an acceptable level. Bechert et al. (2000) demonstrate that additional holes, slits and especially the pattern of dragonfly wings lead to reduced drag on the HQ17 airfoil at $Re = 1.0 \cdot 10^6$. In addition, promising results are presented for very small GF-heights in the range of 0.2 %c < GF < 0.5 %c, i.e. substantially smaller than the BL thickness at the TE. Following from that, CFD-based wake simulations of Schatz et al. (2004) reveal that the amount of induced drag depends on the GF-height, in fact, in a disproportionate manner, illustrated in Figure 2 (b). As such, for GF = 1.5 %c a vortex street is triggered while for GF = 0.5 %c the wake is shed in a relatively smooth way. In a similar manner, Alber et al. (2017) suggest the use of very small GF-heights of approximately half the local BL thickness in order to maintain, or even improve, the airfoil L/D-ratio of different DU and NACA airfoils.

The aforementioned design principles are applied on a research turbine using GF-heights of 0.5 %c and 1.0 %c. In addition, forced LE transition is triggered in order to emulate roughness effects. Subsequently, the impact of retrofit GFs is investigated based on the following experiments:

- 3D Ultrasonic Anemometry in the turbine wake to determine the local AoA.
- Pressure taps in the mid-span blade region to determine the local pressure distribution and lift performance.

- Strain gauges at the blade root to determine the flapwise and the edgewise root bending moments.

In the remaining of this paper, the experimental set-up is described in detail, followed by the presentation and the discussion of the results. The main conclusions are summarized in the final section of this report.

2 Experimental set-up

2.1 Berlin Research Turbine

The Berlin Research Turbine (BeRT) is a test bench of the closed-loop wind tunnel of the Hermann-Föttinger Institut at the Technische Universität Berlin. It is a unique wind turbine demonstrator to explore specific fluid-dynamic phenomena based on a fully equipped rotating system, as detailed by Vey et al. (2015).

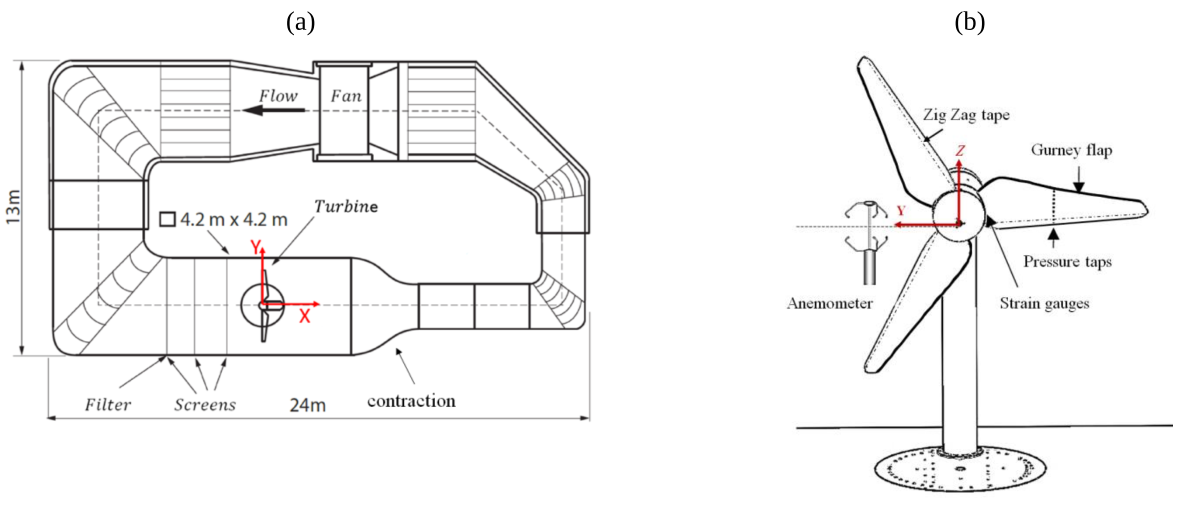

Figure 3. (a) Closed-loop wind tunnel in top-view. (b) BeRT set-up in front-view looking downstream.

Figure 3 (a) depicts the wind tunnel facility consisting of the high speed ($2.0 \cdot 1.4$ m^2) and the low speed ($4.2 \cdot 4.2$ m^2) test section. The BeRT is situated in the low speed test section downstream of the flow-conditioning screens and upstream of the wind tunnel contraction. The maximum inflow velocity is 10 ms^{-1}. The third screen upstream the rotor plane is equipped with an additional turbulence filter mat (Vildedon P15/150s) in order to reduce the turbulence intensity to $1.0\ \% < Ti < 1.5\ \%$, previously reported by Bartholomay et al. (2017). Figure 3 (b) displays the BeRT set-up and the measurement methods applied. The rotor radius is $R = 1.5$ m producing a relatively large blockage ratio of approximately 40 %. Relative distances are expressed in relation to the rotor radius, R, and the zero position at the center of the rotor plane at $X = Y = Z = 0$. The blades consist of the low Reynolds profile Clark-Y with a maximum thickness of $th_{max} = 11.9$ %c and a modified TE thickness of 0.75 %c. The blade geometry is optimized aerodynamically including a linear decrease of both the chord-lengths and the twist-angles from root to tip alongside most of the blade span. The root section is contiguous to the round rotor hub and the tip section is pointy, see Figure 4. The tip speed ratio at rated conditions is $TSR = 4.3$ developing a span-wise Reynolds number range from root to tip of $1.7 \cdot 10^5 < Re < 3.0 \cdot 10^5$. The axial inflow velocity is captured by two parallel Prandtl tubes that are permanently installed at approximately one rotor radius upstream, close to each wind tunnel wall and slightly above hub-height. At rated conditions, the inflow velocity is 6.5 ms^{-1} at a rotational frequency of f_{rot} = 3 Hz. The Data Acquisition (DAQ) system of the rotating sensors, such as pressure taps and strain gauges, is installed within the rotational spinner, displayed in Figure 6 (a). The electrical power is transferred to the rotating system through a slip ring. Communication with the host PC is established via WIFI connection in order to set and modify the rotational speed. The DAQ system captures all channels simultaneously at 10 kHz generating around $6.0 \cdot 10^5$ data points per measurement that are streamed to a host PC via network connection.

2.2. Blade configurations and operation points

2.2.1 Forced transition

The principal baseline configuration of the BeRT includes Zig Zag (ZZ) turbulator tape (Klein et al., 2018), in short, the tripped case. ZZ tape is applied in order to initiate the laminar-to-turbulent transition of the Boundary Layer (BL) at a fixed location. In practical terms, it is used to emulate LE roughness effects on airfoil sections (Rooij and Timmer, 2003) as well as rotor blades (Zhang et al., 2017). Its height is slightly smaller than the local BL thickness in order to trigger the BL transition while avoiding the disproportionate drag increase or even turbulent separation. The ZZ tape is implemented on all BeRT blades at a chord-wise LE position of both the Suction Side (SuS) at x_{SuS} = 5.0 %c and the Pressure Side (PrS) at x_{PrS} = 10.0 %c. The BL thickness of the clean baseline, δ, is calculated with XFOIL, developed by Drela (1989) based on the Reynolds number, the AoA and the N-criterion (Ncrit) modeling the transition location. The design conditions are defined by α_{opt} =5.0°, $Re = 2.5 \cdot 10^5$ and Ncrit = 6 representing the elevated *Ti* inside the test section. Depending on δ, the absolute height of the ZZ tape is adjusted in various steps in relation to the chord-length, depicted in Figure 4 (a). In addition, all experiments are performed under the consideration of the free BL transition, in short, the clean case, i.e. without including ZZ tape.

2.2.2 Gurney flaps

The GF-height is submerged by the BL at the TE in order to keep the induced drag penalty on an acceptable level. Considering design conditions, XFOIL predicts the BL thickness at the TE to be δ_{TE} = 1.0 %c. Furthermore, another GF-height of half the local δ is chosen, so that the GF configurations include *GF* = 1.0 %c and *GF* = 0.5 %c. Apart from the very tip section, they are implemented in the form of thin angle profiles made of brass. One side of the angle profiles is cut in a linear way in order to match the chord decrease, shown in Figure 4 (b). The other side of the profile is attached with thin double-sided adhesive tape adjacent to the TE.

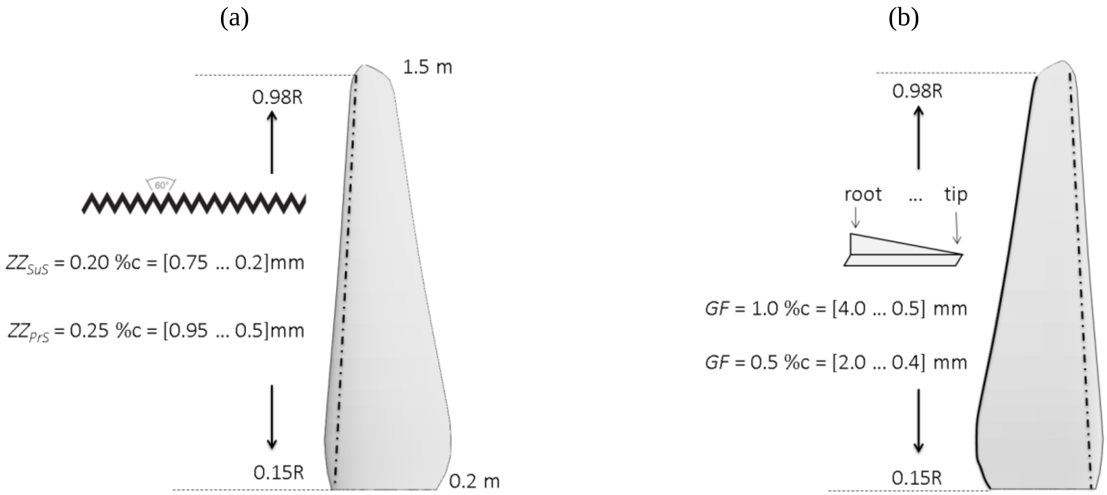

Figure 4. (a) Zig Zag tape at the leading edge of the suction side. (b) Gurney flap and ZZ tape at the pressure side of the trailing edge.

2.2.3 Test matrix

Table 1 summarizes the test matrix that consists of four blade configurations, three Operation Points (OPs) and three measurement methods. The OPs include the so-called stall, rated and feather conditions, which are characterized by low, medium and high TSR or AoA, respectively. Each measurement has a total duration of 60 s. No blockage correction is applied, so that the results refer to the conditions inside the closed test section. All sensors are calibrated and an zero-offset measurement is performed before each test-run in order to reduce experimental errors. The uncertainty of the results is evaluated in Appendix B.

Table 1. Test matrix

Blade configuration		
	Tripped baseline	Clean baseline
GF = 0.5 %c	Operation points	
GF = 1.0 %c		
Measurement method		
Ultrasonic anemometry	Wake-velocities → AoA	
Pressure taps	c_p distribution → lift curve	
Strain gauges	Root bending moments	

Operation point (clean case)			
	Stall	Rated	Feather
TSR	3.0	4.3	5.6
Inflow velocity in ms^{-1}	6.5	6.5	5.0
Rot. frequency in Hz	2.1	3.0	3.0
AoA in ° (Sect. 3.1)	16.5	8.6	4.6
Re-number (Sect. 3.2)	$2.2 \cdot 10^5$	$2.8 \cdot 10^5$	$2.7 \cdot 10^5$

The Re-numbers, see Table 1, are determined by means of the experimental method that is laid-out in Sect. 2.3. They are significantly lower compared to the Re-numbers of several millions that occur along the blades of multi-MW HAWTs. Nonetheless, the effectiveness of the Gurney flap is determined by the ratio between its height and the corresponding boundary layer thickness, especially in terms of the resulting L/D ratio, see Figure 2 (b). Hence, the present findings are considered relevant beyond the Re-numbers of the BeRT blades, as long as the GF/BL ratio is kept constant.

2.3 Measurement methods

The measurement methods listed in Table 1 consist of three types of sensors that are simultaneously recording the wake velocity, the pressure distribution and the root bending moments.

2.3.1 Ultrasonic anemometry

3D Ultrasonic Anemometers (UAs) are widely spread in the wind energy industry. The technology is recognized by different wind industry standards such as the IEC 61400 to determine the power curve of wind turbines or the Association of German Engineers (VDI) for turbulence measurements. Moreover, there are numerous references for the use of UAs in the context of wind tunnel campaigns, such as Weber et al. (1995), Hand et al. (2001) and Cuerva et al. (2003). The UA is a commercial product of Thies CLIMA (version 4.383). According to the manufacturer, they are pre-calibrated and free from maintenance.

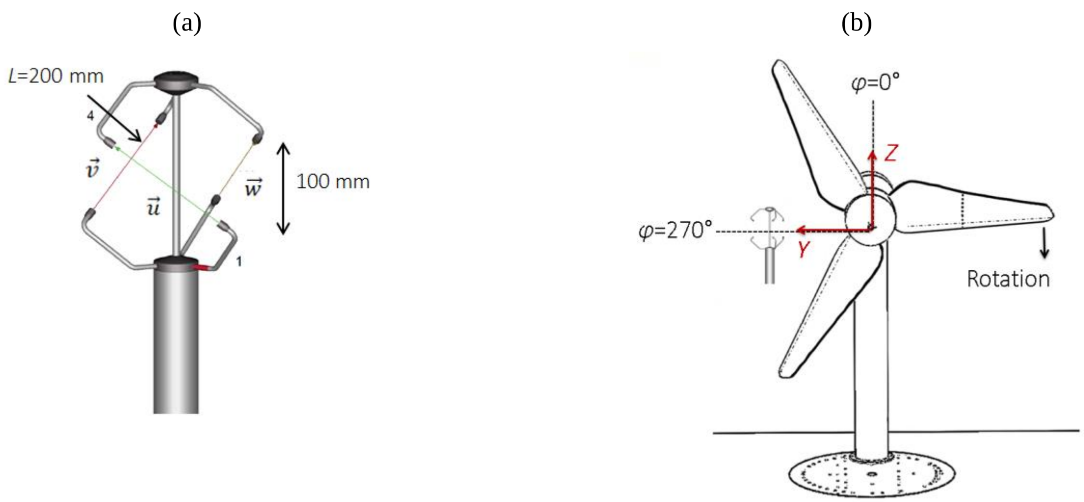

Figure 5. (a) Ultrasonic Anemometer, reproduced and modified from Thies CLIMA. (b) Definition of the azimuthal blade positions looking downstream.

Figure 5 (a) displays the three separate acoustic transmitter-receiver pairs that are installed orthogonally to each other. The velocity vectors, $\vec{u}$, $\vec{v}$ and $\vec{w}$, are determined by six individual measurements based on the bidirectional time-of-flight principle, i.e. the duration of each signal to be sent and received,

$$\vec{u} = \frac{L}{2}\left(\frac{1}{t_1} - \frac{1}{t_2}\right), \tag{1}$$

where L = 200 mm is the exact running-length between each sensor pair, so that the measurement volume amounts to $100 \cdot 200 \cdot 200\ mm^3$. The velocity vectors $\vec{v}$ and $\vec{w}$ are determined accordingly. Eq. (1) shows that the 3D velocity calculation depends solely on the average propagation time of the ultrasound, t_1 and t_2, depending on the specific airflow passing through the measurement volume. As such, the output values already imply the density and temperature of the air. Subsequently, the velocity vectors are transformed into a natural coordinate system, so that the output time-series consist of the axial, lateral and vertical velocity components, *u*, *v* and *w*. The device-internal DAQ system is a half-duplex interface that is completely independent of both the wind tunnel and the BeRT system. According to the manufacturer, the measurement accuracy is 0.1 ms^{-1} per integrated value and 0.01 ms^{-1} with respect to each of the three velocity components. The data is recorded at a sampling rate of 60 Hz thus providing around 3600 data points per measurement. Considering the relatively large measurement volume and the low sampling rate compared to e.g. hotwire or laser-based devices, the UA is not adequate for the investigation of complex or high-speed flow structures. However, the BeRT wake-flow is expected to consist of an axial and a tangential velocity component due to the formation of a rotating wake tube. The impact of complex tip and root vortices is considered negligible in the mid-span blade region, as shown by Herráez et al. (2018).

The UA is installed at one static position downstream, X = 1.3R, in the mid-span region, Y = 0.56R, and at hub height, Z = 0R, see Figure 5 (b). It is positioned vertically with a spirit level and turned around its own axis towards the undisturbed axial inflow, so that the lateral and the vertical components, *v* and *w*, tend to zero. The set-up is fixed at its final position for all measurements, which are presented in Sect. 3.

2.3.2 Pressure taps

The pressure distribution is extracted by means of 18 Pressure Taps (PTs) on the SuS and 12 on the PrS, located along the chord-length at r = 0.45R, see Figure 6 (b). Each orifice is connected via silicone tubing to its corresponding differential pressure sensor (HCL0025E), i.e. the pressure box inside the spinner. The sensor accuracy is given with 0.05 % of the full scale range of ± 2500 Pa under nominal conditions. The experimental procedure and the data post-processing is based on Soto-Valle et al. (2019).

(a) (b)

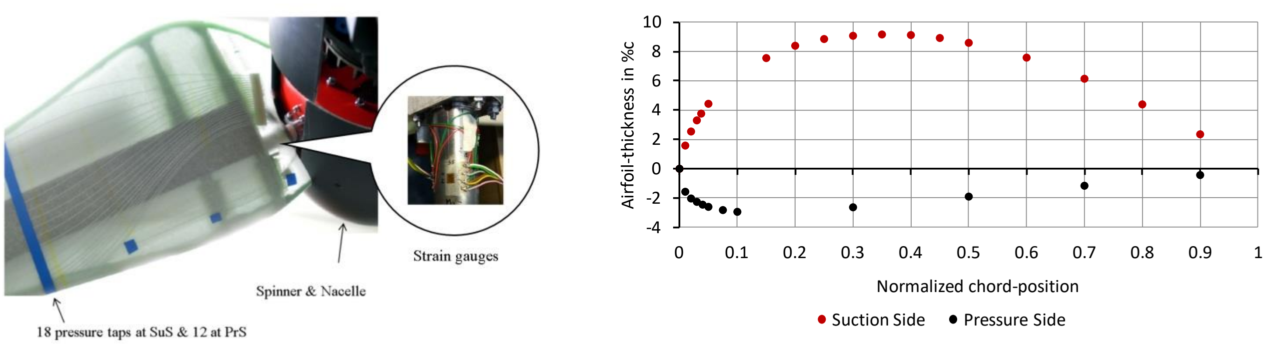

Figure 6. (a) BeRT blade and pressure taps, reproduced and modified from Fischer (2015). (b) Chord-wise position of pressure at r = 0.45R.

The differential pressure values are transformed into the pressure coefficient,

$$c_{pi} = \frac{\Delta p_{sti} + p_{rot}}{p_{dyn,ref}} = \frac{(p_{sti} - p_{st,\infty}) + (0.5\rho \cdot (\omega r)^2)}{p_{dyn,ref}}\,, \tag{2}$$

where

- Δp_{sti} is the static pressure difference between each PT and the inflow Prandtl tube $p_{st,\infty}$.
- p_{rot} refers to the pressure due to the rotation of the blade element. It is added to Δp_{sti} in the form of a constant correction term in accordance with Hand et al. (2001).
- $p_{dyn,ref}$ describes the referential dynamic pressure, i.e. the effective flow velocity experienced by the blade element. Following Hand et al. (2001), it is determined by the maximum pressure that is recorded on the pressure side, the frontal stagnation point, where $c_{pi} = 1.0$. According to Eq. (2) the referential dynamic pressure is then determined by $p_{dyn,ref} = \Delta p_{st,ref} + p_{rot}$.

The c_p values are phase-averaged over an azimuthal angle of $\varphi = 10°$ (Figure 5 (b)). Each PT provides a total of 36 pressure values at the following blade positions: $\varphi = [0°, 10°, 20° \ldots 350°]$, so that $\varphi = 270°$ contains the average of all data points between $265° < \varphi < 275°$. The pressure difference, Δc_p, is calculated by subtracting the integrated c_p distribution between the PrS and the SuS in order to determine both the normal coefficient, c_n, and the tangential coefficient, c_t. Per definition, $\overrightarrow{c_n}$ is orthogonal to the chord-line pointing towards the SuS, while $\overrightarrow{c_t}$ is parallel to the chord-line pointing towards the LE.

According to Hand et al. (2001),

$$c_n = \frac{1}{2} \cdot \sum_{i=1}^{30} \cdot \left(c_{pi} + c_{pi+1}\right) \cdot (x_{i+1} - x_i), \tag{3}$$

and

$$c_t = \frac{1}{2} \cdot \sum_{i=1}^{30} \cdot \left(c_{pi} + c_{pi+1}\right) \cdot (y_{i+1} - y_i), \tag{4}$$

where x and y are the normalized chord positions of each PT. The numbering starts at the TE ($x = 0.9$) with the 18 PTs on the SuS moving anti-clock wise until the LE ($x = 0$) and back to the TE on the PrS.

Subsequently, the lift coefficient, c_l, is determined by

$$c_l = c_n \cdot \cos(\alpha) + c_t \cdot \sin(\alpha). \tag{5}$$

The required AoA, α, are adopted by the uncorrected inflow and wake velocity measurements (Sect. 3.1). The term $c_t \cdot \sin(\alpha)$ in Eq. (5) solely describes the pressure drag, which does not contain the skin-friction drag, so that $c_t \cdot \sin(\alpha) < c_d$. Moreover, for relatively small AoA, $c_t << c_n$ (Barlow, 1999).

2.3.3 Strain gauges

The Strain Gauges (SGs) are mounted at the clamping of the blade (Figure 6 (a)) detecting the Root Bending Moments (RBMs) in the out-of-plane or flapwise and in-plane or edgewise direction. They are connected in a full-bridge configuration aiming at the mitigation of temperature and cross talk effects (FAET-A6194N-35). The experimental procedure to determine the RBMs is based on Bartholomay et al. (2018). For the purpose of the presented baseline measurements, a simplified post-processing protocol is applied without including the data-based cross talk correction.

Before testing each blade configuration, the offset signal is recorded in slow-motion at the lowest rotating frequency available, f_{rot} = 0.1 Hz. In this way, the gravitational RMBs are subtracted from the results, which are otherwise registered as a sinusoidal signal in the edgewise direction. At operational frequencies, the axial forces due to the blade rotation are causing a material deformation directed towards the blade tip. They are quantified as a combination of centrifugal and gravitational forces by

$$F_{axial} = F_{cent} - F_{grav} = \left(m_{blade} \cdot r_{cg} \cdot \omega^2\right) - \left(m_{blade} \cdot g \cdot \cos(\varphi)\right), \tag{6}$$

where m_{blade} = 5.67 kg, the center of gravity is located at r_{cg} = 0.31R, g is the gravitational constant and φ refers to each phase-locked blade position. The rotational frequency, ω, is kept constant during each test-run so that the centrifugal force F_{cent} becomes a constant correction term at each OP. The effective flapwise and edgewise RBMs, which are related exclusively to the aerodynamic loads acting on the blade, are determined by

$$M_{flap}(\varphi) = \left(U_{\mathrm{f,raw}}(\varphi) - U_{f,off}(\varphi)\right) \cdot \mathrm{K}_{f1} - \left(F_{axial} \cdot \mathrm{K}_{f2}\right), \tag{7}$$

and

$$M_{edge}(\varphi) = \left(U_{\mathrm{e,raw}}(\varphi) - U_{e,off}(\varphi)\right) \cdot \mathrm{K}_{e1} - (F_{axial} \cdot \mathrm{K}_{e2}), \tag{8}$$

where

- M_{flap} and M_{edge} are the aerodynamic flapwise or edgewise RBMs in Nm.
- $U_{f,raw}$ and $U_{e,raw}$ stand for the raw data signal in V.
- $U_{f,off}$ and $U_{e,off}$ describe the slow-motion offset signal in V.
- K_{f1} and K_{e1} refer to constant calibration factors to transform V into Nm.
- K_{f2} and K_{e2} refer to constant calibration factors to transform the axial forces from N into Nm.

Applying Eq. (7) and (8) both the out-of-plane and the in-plane RBMs are computed for each of the 36 blade positions, as shown in Sect. 3.

3 Results

The results of both the tripped and the clean cases are presented and discussed. For space economy, the clean case is only included in terms of the concluding results, such as the lift performance in Sect. 3.2 and the root bending moments in Sect. 3.3, but otherwise accessible in Appendix A for completeness.

3.1 Wake velocities and angles-of-attack

Following Snel et al. (2009), Figure 7(a) shows the axial and tangential wake velocity normalized by the axial inflow velocity at each OP, uu_{∞}^{-1} and wu_{∞}^{-1}.

(a) (b)

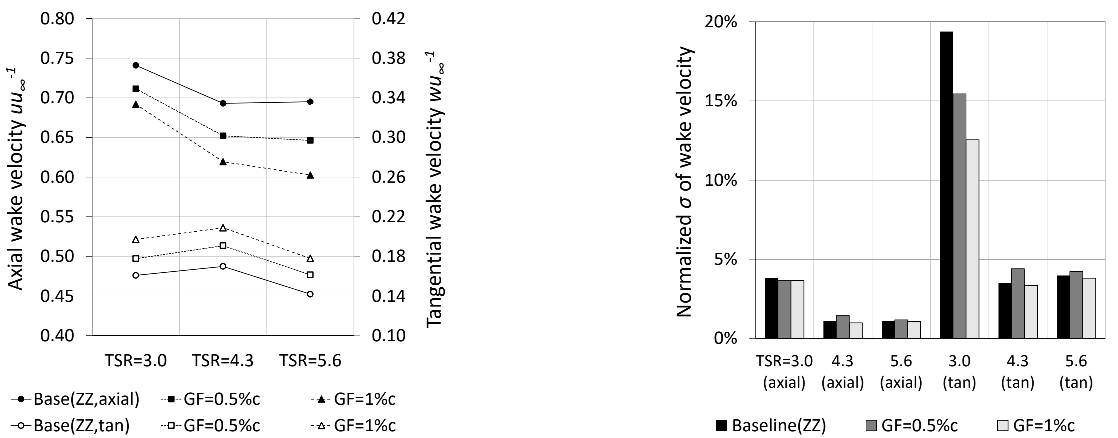

Figure 7. Tripped case at r = 0.56R and φ = 270°. (a) Axial and tangential wake velocity normalized by the inflow velocity. (b) Standard deviation of the wake velocity normalized by the average wake velocity.

Starting from the baseline, the axial wake velocities are found to be significantly higher compared to typical free flow conditions (Figure 7 (a)). According to the steady state Blade Element Momentum (BEM) method, the optimum axial wake velocity is supposed to be around one third of the inflow (Burton, 2011). In this case, it amounts to more than two thirds at all OPs. This phenomenon is caused by the wind tunnel blockage effects, previously shown by CFD simulations using the fluid dynamic code FLOWer. At rated conditions of the BeRT, Klein et al. (2018) conclude that the flow decelerates to an axial wake velocity in the range of $0.62u_{\infty} < u_{CFD} < 0.77u_{\infty}$, which is in agreement with the experimental results, $u_{EXP} = 0.69u_{\infty}$. Furthermore, the corresponding tangential velocity is similar to the steady state BEM simulation of QBlade with $w_{BEM} = 0.18u_{\infty}$ compared to $w_{EXP} = 0.17u_{\infty}$ (Marten et al., 2013). Hence, the tangential wake velocity is relatively close to the standard BEM simulation, despite the influence of the wind tunnel walls.

Regarding the impact of the GFs, Figure 7 (a) illustrates the consistent decrease of the axial, and the consistent increase of the tangential wake velocity both in relation to the GF-height. The lateral velocity component is neglected as it amounts to $v \ll$

$|\pm 0.1\ ms^{-1}|$. Figure 7 (b) summarizes the standard deviation normalized by the corresponding average velocity component, as such describing the 1D turbulence intensity, expressed in percent (Burton, 2011). As expected, the flow separation is captured by the UA in the form of a more turbulent wake field, especially regarding the tangential component. The GF configurations do not influence the wake turbulence considerably, except for the tangential velocity component at stall, *TSR* = 3.0, where the GFs appear to mitigate the turbulence level.

Next, the wake velocity is converted into the axial and tangential rotor induction factors,

$$a = \frac{1}{2}\left(1 - \frac{u}{u_\infty}\right), \tag{9}$$

and

$$a' = \frac{w}{2\omega r}. \tag{10}$$

The induction factors, *a* and *a'*, describe the decrease of the axial, and the increase of the tangential velocity component from a reference point sufficiently far away from the rotor plane rather than the rotor plane itself (Burton 2011). The wake measurements are taken at a distance of *X* = 1.3R downstream in order to avoid the influence of the wind tunnel contraction, see Figure 3 (a). According to Hansen (2015) and Eq. (9) and (10), the AoA is derived from

$$\alpha = \arctan\left(\frac{(1-a)\ u_\infty}{(1+a')\ \omega r}\right) - \beta = \arctan\left(\frac{u_\infty + u}{2\omega r + w}\right) - \beta, \tag{11}$$

where the twist-angle at the radial location of the UA is β (0.56R) = 9.8°.

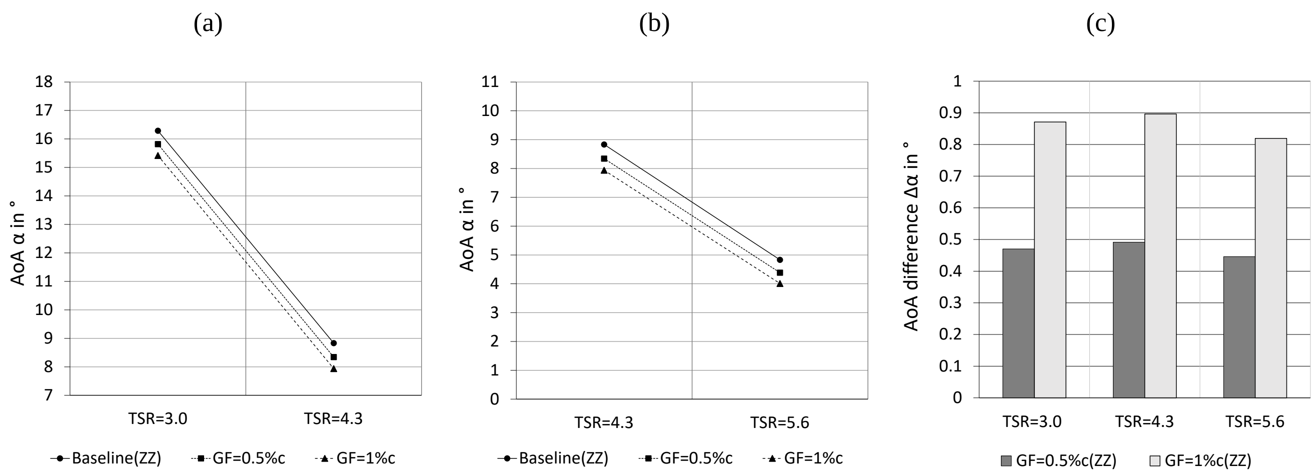

Figure 8. Angles-of-attack in the tripped case at *r* = 0.56R and φ = 270°. (a) Stall and rated conditions (b) Rated and feather conditions (c) AoA difference between Gurney flap configuration and the baseline.

At rated conditions, the AoA of the baseline case is α_{ZZ} = 8.8°, see Figure 8 (a) and (b). This outcome is in agreement with previous investigations based on 3-hole probes as well as CFD simulations of the BeRT, detailed by Klein et al. (2018). Hence, the AoA are considered stable with respect to the mid-span region, i.e. 0.65R < r < 0.45R. Furthermore, Figure 8 (c) displays the consistent AoA decrease caused by the GF configurations. Depending on the GF-height, it amounts to $\Delta\alpha_{GF=0.5\%c}$ = 0.5° and $\Delta\alpha_{GF=1.0\%c}$ = 0.9°, i.e. to a more favorable level in terms of the BeRT rotor. Hence, the results quantify a crucial effect of retrofitted GFs on the blade performance; decreasing axial wake velocities and thus reduced AoA.

In the following Sect. 3.2, the AoA are correlated to the normal force coefficients, c_n, in order to obtain the lift coefficients, c_l.

3.2 Pressure distribution and lift performance

Figure 9 shows the distribution of the pressure coefficients, c_p, regarding the different OPs.

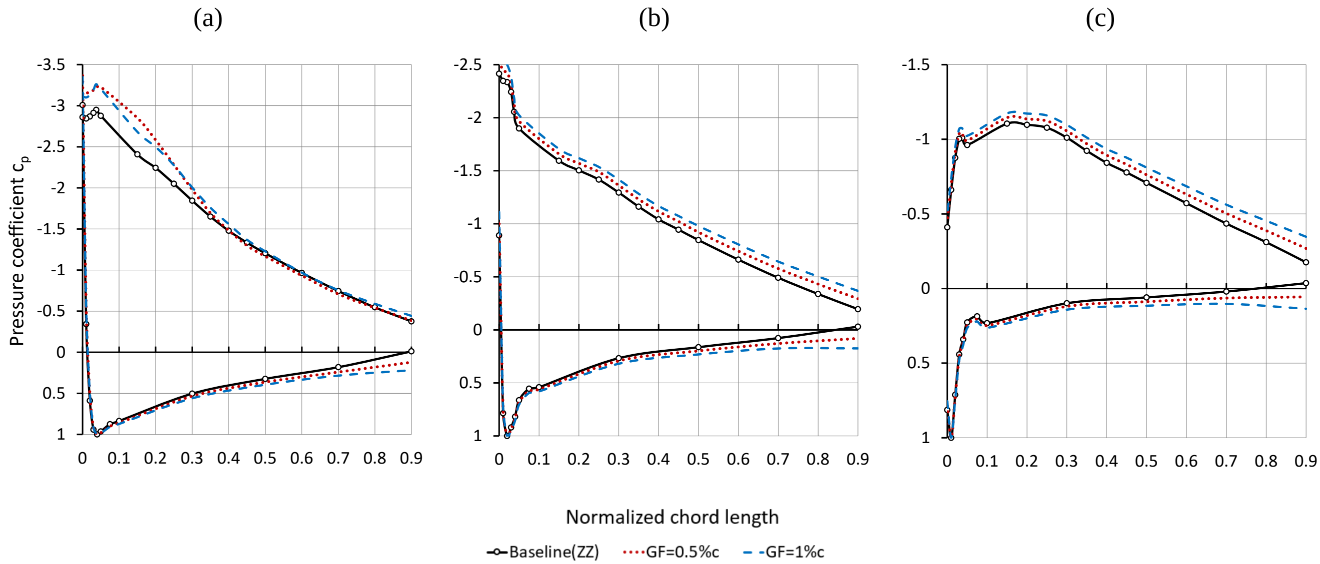

Figure 10. Pressure distribution in the tripped case with respect to different scales at r = 0.45R and φ = 270°. (a) TSR = 3.0. (b) TSR = 4.3. (c) TSR = 5.6.

The relative pressure difference, Δc_p , expands along the complete chord length when applying GFs. This effect is particularly visible in terms of the aft-loading towards the TE at 0.7 < x < 0.9. In fact, the aft-loading tail is one of the main design approaches in order to improve the roughness sensitivity of the DU airfoils (Rooij and Timmer, 2003). At stall, TSR = 3.0, the separation at the SuS is not complete, despite the elevated AoA, α_{ZZ} = 16.3°. Compared to XFOIL simulations (Sect. 2.3.1), the maximum lift coefficient of the Clark-Y airfoil is already reached at $c_{l,max}$ ≈ 14.0°. Hence, the c_p curves seen in Figure 10 (a) indicate the effect of stall delay due to the blade rotation, as discussed hereafter. In order to quantify the results, the c_p distribution is transformed into the local lift curve based on Eq. (5). The required AoA are adopted from Sect. 3.1, so that the lift coefficients combine the results of both the wake-velocity and the pressure measurements.

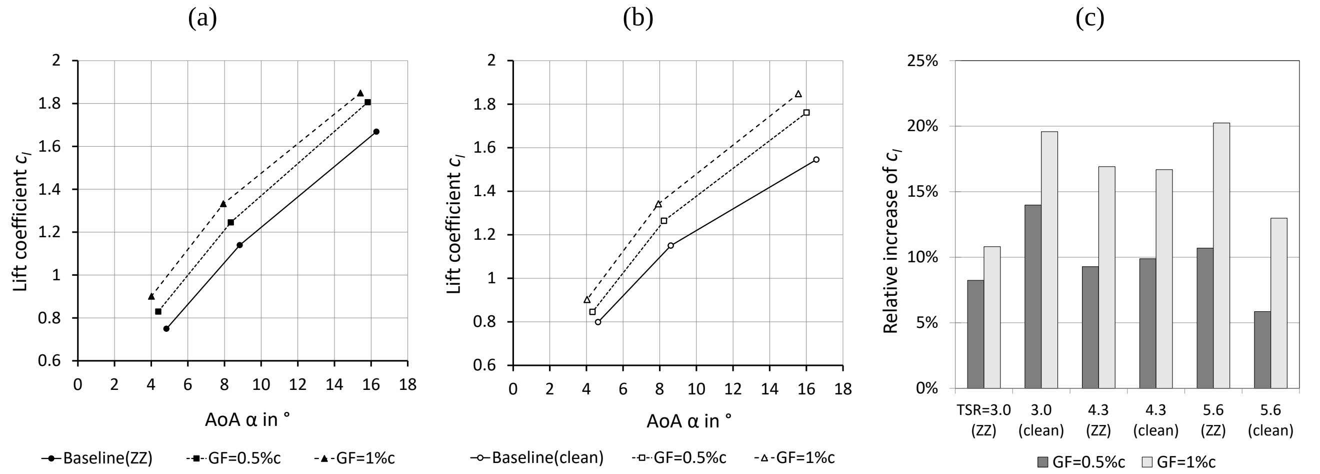

Figure 11. Lift coefficients over angle-of-attack at r = 0.45R and φ = 270°. (a) Tripped case. (b) Clean case. (c) Relative lift increase of Gurney flap configurations in relation to the corresponding baseline.

Figure 11 (a) and (b) depict the lift coefficients of both the tripped and the clean cases. Starting from the baseline, the tripped case shows smaller c_l at 4° < α < 5° because of the forced BL transition at the LE. At 8° < α < 9°, this is not the case anymore, while in the stall region, 15° < α < 17°, the ZZ tape appears to develop a beneficial effect on the lift performance. This phenomenon is probably caused by the tripped and more turbulent BL that remains attached until closer to the TE. In the clean case, however, the less energetic BL separates earlier thus leading to smaller c_l at elevated AoA. This observation is confirmed by comparable airfoil experiments on the FX 63-137 airfoil section at $1.0 \cdot 10^5 < Re < 2.0 \cdot 10^5$ using ZZ tape with a thickness of 0.75 mm (Holst et al. 2016). Despite the decrease in the pre-stall, the lift coefficients are found on a similar level in the post-stall region.

Furthermore, looking at the GF configurations (Figure 11 (a) and (b)), the lift performance in the tripped case is on a similar, or even higher level considering the complete AoA range, 4° < α < 17°. Hence, forced LE transition is not mitigating or neutralizing the GF effect. In fact, the GF configurations appear to alleviate the adverse effects of LE roughness by improving the local lift performance. Figure 11 (c) summarizes the relative c_l increase of both GF configurations in relation to the corresponding baseline cases. At rated conditions, TSR = 4.3, $\Delta c_{l,GF=0.5\%c}$ = 0.11 or 9.3 % and $\Delta c_{l,GF=1.0\%c}$ = 0.19 or 16.9 %, illustrating the main characteristic of retrofit GFs; the considerable lift increase.

Moreover, the scale of Δc_l is in agreement with comparable wind tunnel experiments based on a Clark-Y airfoil section, as depicted in Figure 12.

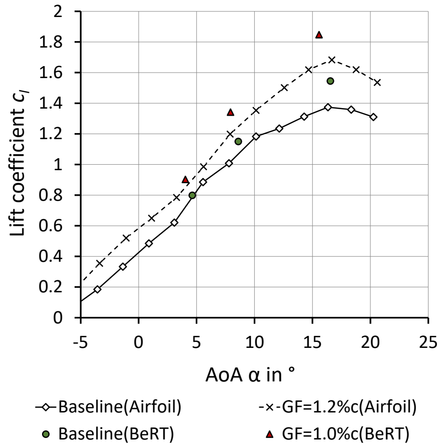

Figure 12. Lift coefficients of a Clark-Y airfoil including Gurney flap, reproduced from Kheir-Aldeen (2014).

Figure 12 compares the lift coefficients of the clean Clark-Y airfoil section (th_{max} = 14.0 %c, $Re = 2.1 \cdot 10^5$, GF = 1.2 %c) and the clean Clark-Y blade element of the BeRT (th_{max} = 11.9 %c, $Re = 2.5 \cdot 10^5$, GF = 1.0 %c). The results demonstrate similarities for both the baseline and the GF configurations. The elevated c_l in case of the BeRT are due to the thinner Clark-Y blade element. At $c_{l,max}$, the blade performance is furthermore characterized by the radial flow due to the blade rotation causing stall delay. This behavior is in agreement with experiments on the field rotor at the Delft University of Technology. Rooij and Timmer (2003) report a significant shift of $c_{l,max}$ compared to 2D airfoil simulations.

After evaluating one area of the mid-span blade region, the impact of GFs over the complete blade span is presented in Sect 3.3

3.3 Root bending moments

The integration of the aerodynamic loads, i.e. the lift and the drag forces acting along the blade span, yield the RBMs. The in-plane or edgewise RBMs are proportional to the rotor torque and thus the mechanical power output. They are directly related to the out-of-plane or flapwise RBMs, which are proportional to the rotor thrust and thus the structural loads (Hansen, 2015).

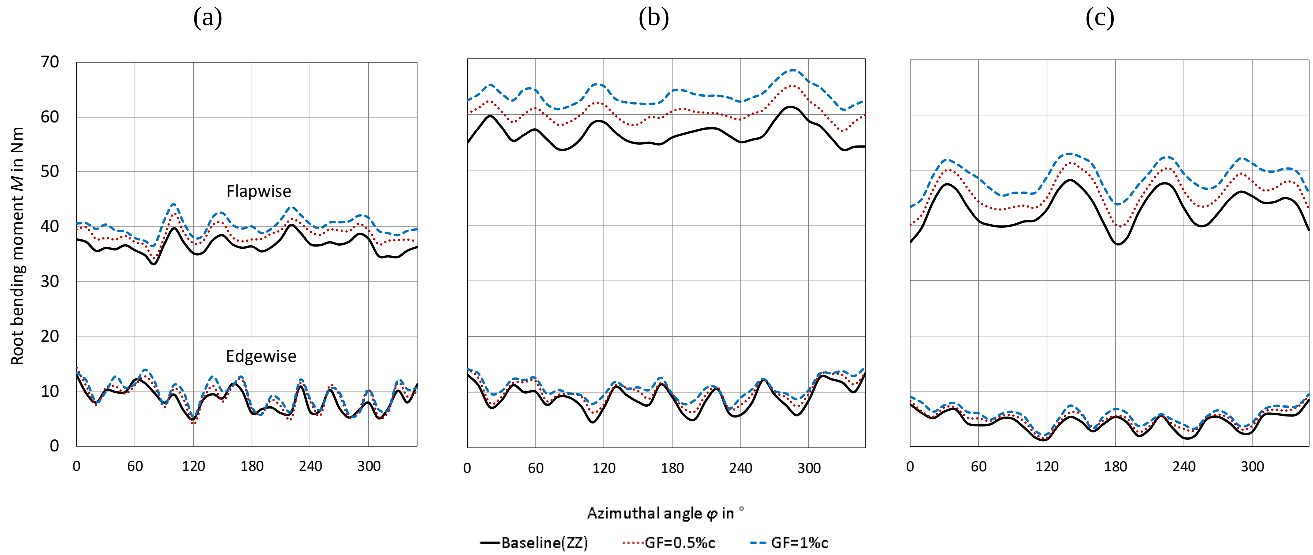

Figure 13. Flapwise and edgewise root bending moments in the tripped case. (a) *TSR* = 3.0. (b) *TSR* = 4.3. (c) *TSR* = 5.6.

Figure 13 displays the aerodynamic RBMs that are recorded over one blade revolution in the form of 36 phase-locked blade positions. The impact of the GF configurations is registered as an overall increase of both the flapwise and the edgewise RBMs. In order to quantify and to discuss the results, the RBMs are presented as average values for both the tripped and the clean cases.

(a) (b)

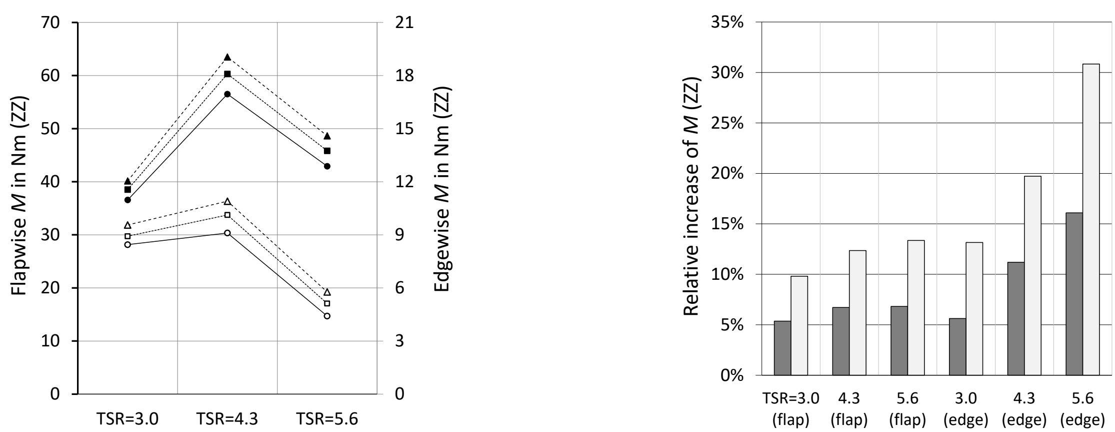

(c) (d)

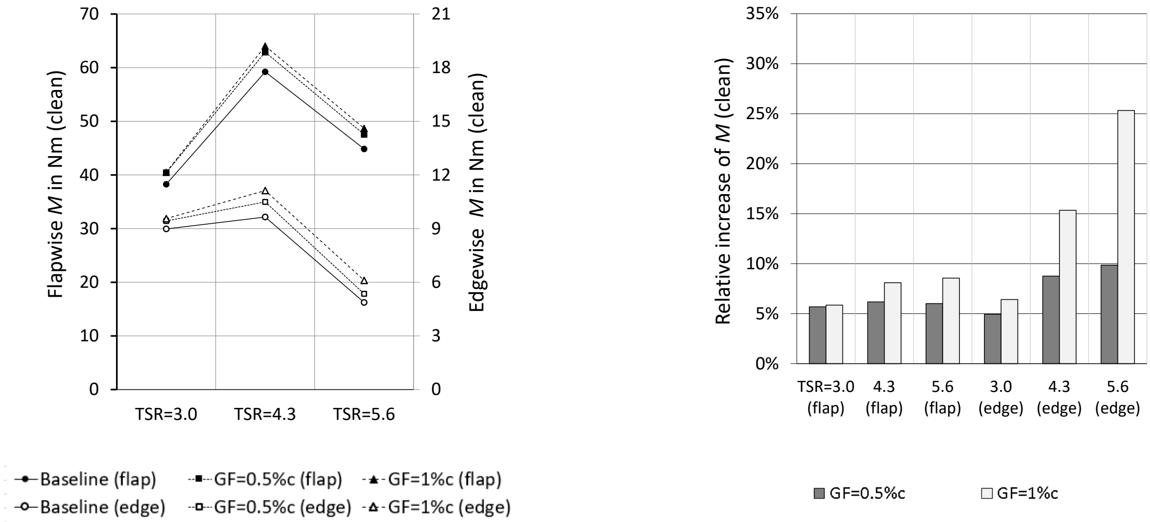

Figure 14. Flapwise and edgewise root bending moments. (a) Tripped case. (b) Relative increase to tripped baseline. (c) Clean case. (d) Relative increase to clean baseline.

The results of Figure 14 (a) confirm the increment of the average RBMs in relation to the GF-height in accordance with the previous Figure 13. In the clean case, the overall trend is similar to the tripped case considering all OPs, see Figure 14 (c). This means that the impact of the Gurney flaps, previously quantified in terms of the local lift coefficients, is now registered in the form of increased RBMs in both the flapwise and the edgewise direction.

In Figure 14 (b), the performance of the GF configurations is quantified in relation to the tripped baseline. At rated conditions, the average increase of the flapwise RBMs amount to $\Delta M_{\mathrm{flap,GF=0.5\%c}}$ = 3.8 Nm or 6.7 % and to $\Delta M_{\mathrm{flap,GF=1.0\%c}}$ = 7.0 Nm or 12.4 %. At the same time, the edgewise RBMs are enhanced by $\Delta M_{\mathrm{edge,GF=0.5\%c}}$ = 1.0 Nm or 11.2 % and $\Delta M_{\mathrm{edge,GF=1.0\%c}}$ = 1.8 Nm or 19.7 %. In the clean case, see Figure 14 (d), the overall trend is similar, however less pronounced. In both cases, the GF configurations generate performance improvements regarding the rotor torque, however at the expense of the inherent increase of the rotor thrust.

Furthermore, the results reinforce the observation that GFs are more effective in relation to the tripped compared to the clean baseline. Looking at the relative increase shown in Figure 14 (b) and (d), the GF configurations appear to alleviate the effects of forced LE transition, especially on the edgewise RBMs, as previously discussed in Sect. 3.2 with respect to the local lift performance.

4 Conclusions

The aerodynamic impact of Gurney flaps is investigated on the rotor blades of the Berlin Research Turbine. The baseline measurements confirm the influence of the prevailing wind tunnel blockage. At rated conditions and in the mid-span blade region, the axial wake velocity is approximately double in comparison to ideal free flow conditions. As such, the corresponding angles-of-attack are elevated in comparison to the design case and amount to α_{exp} = 8.8° rather than α_{opt} = 5.0°.

Under these circumstances, the retrofit application of Gurney flaps leads to performance improvements of both the tripped and the clean cases including tip speed ratios of 3.0, 4.3 and 5.6. At rated conditions, *TSR* = 4.3, the axial wake velocities are reduced and the angle-of-attack are decreased by $\Delta\alpha_{GF=0.5\%c}$ = 0.5° and $\Delta\alpha_{GF=1.0\%c}$ = 0.9°. At the same time, the local lift coefficients are enhanced by $\Delta c_{l,GF=0.5\%c}$ = 0.11 or 9.3 % and $\Delta c_{l,GF=1.0\%c}$ = 0.19 or 16.9 %, which is the main characteristic of Gurney flaps. The effect of the aerodynamic loads over the complete blade span is analyzed by means of the root bending moments. The average increase in the out-of-plane direction amounts to $\Delta M_{\mathrm{flap,GF=0.5\%c}}$ = 3.8 Nm or 6.7 % and to $\Delta M_{\mathrm{flap,GF=1.0\%c}}$ = 7.0 Nm or 12.4 %. Simultaneously, the in-plane bending moments are augmented by $\Delta M_{\mathrm{edge,GF=0.5\%c}}$ = 1.0 Nm or 11.2 % and $\Delta M_{\mathrm{edge,GF=1.0\%c}}$ = 1.8 Nm or 19.7 %. Hence, decreasing angles-of-attack and increasing lift coefficients appear to be correlated with the enhancement of both the rotor torque and the thrust. Furthermore, the aerodynamic impact of Gurney flaps is found more pronounced in the tripped case compared to the clean case. This observation indicates the capacity of Gurney flaps to compensate for the adverse effects of forced LE transition by improving the local lift performance.

In summary, Gurney flaps are considered a passive flow-control device worth investigating for the use on horizontal axis wind turbines. The design of the Gurney flap-height in relation to the local boundary layer thickness is crucial in order to achieve performance improvements while avoiding detrimental effects such as induced drag. Future research is required quantifying the Gurney flap effect on dynamic loads, leading edge roughness and thus the power output of rotor blades that operate in free flow conditions and at high Reynolds numbers.

Appendix A: Results of the clean case

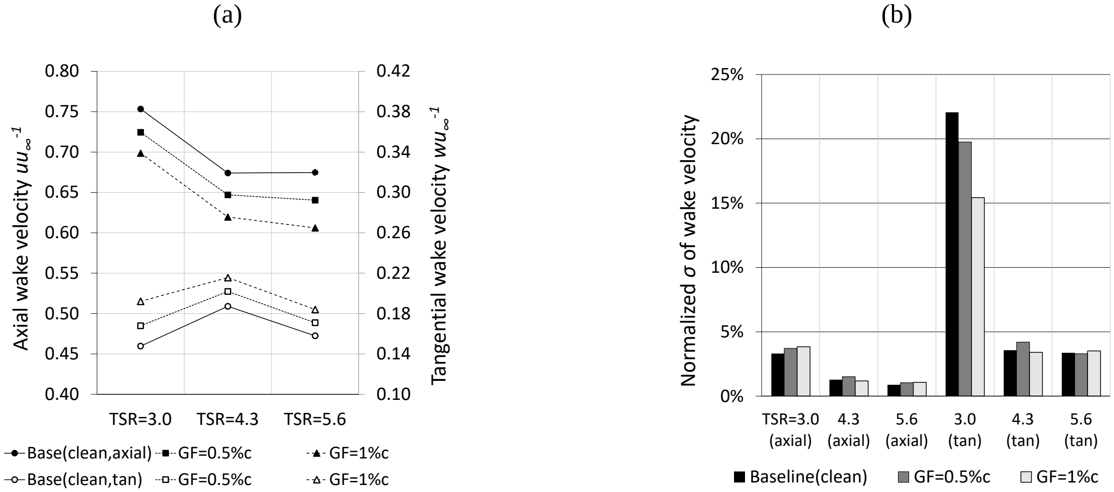

Figure A 1. Clean case at *r* = 0.56R and φ = 270°. (a) Axial and tangential wake velocity normalized by the inflow velocity. (b) Standard deviation of the wake velocity normalized by the average wake velocity.

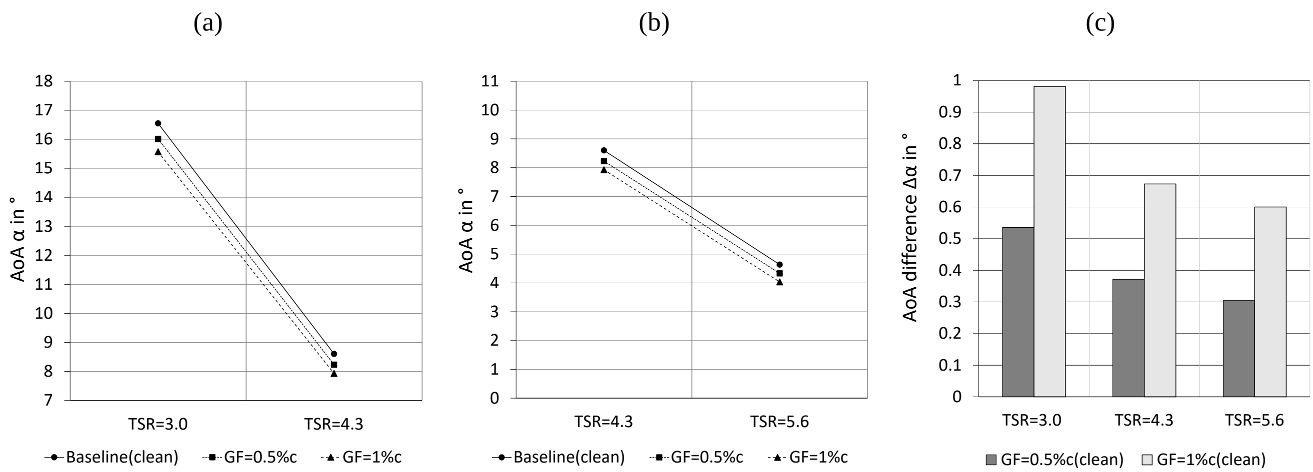

Figure A 2. Angles-of-attack in the clean case at *r* = 0.56R and φ = 270°. (a) Stall and rated conditions (b) Rated and feather conditions (c) AoA difference between Gurney flap configuration and the baseline.

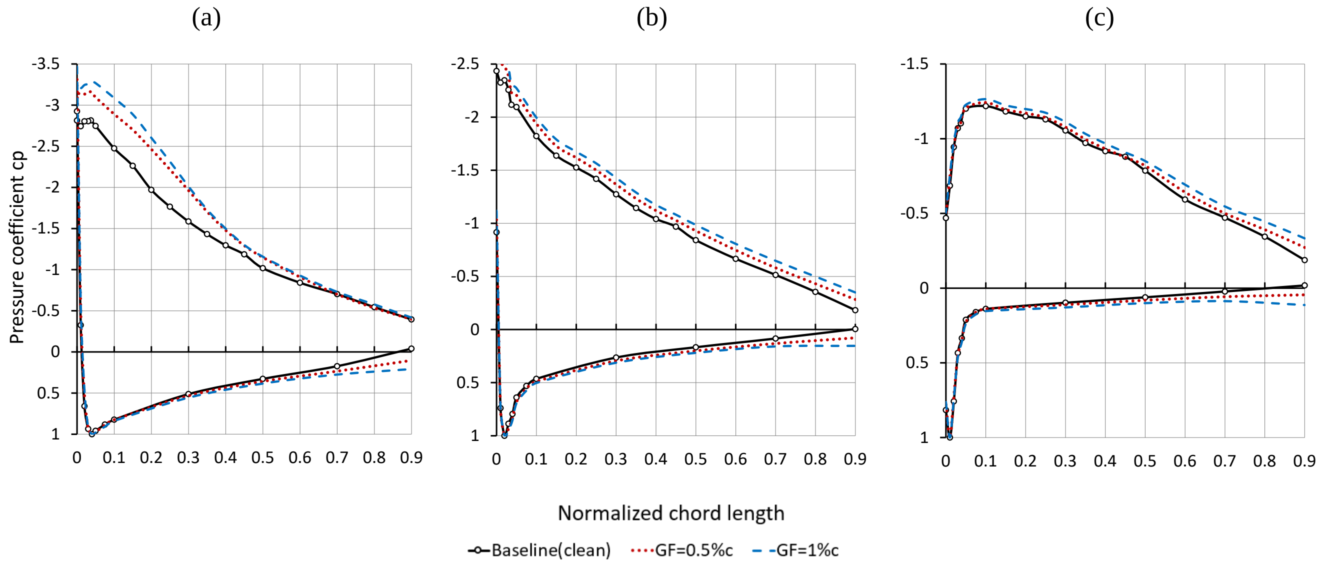

Figure A 3. Pressure distribution in the clean case with respect to different scales at $\boldsymbol{r}$ = 0.45R and φ = 270°. (a) *TSR* = 3.0. (b) *TSR* = 4.3. (c) *TSR* = 5.6.

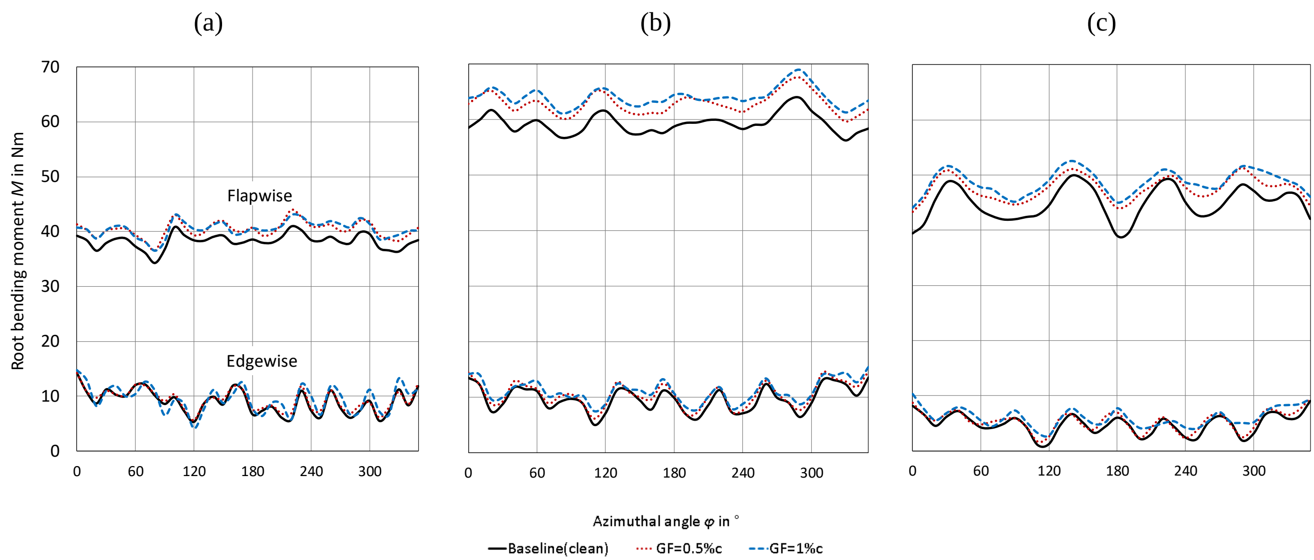

Figure A 4. Flapwise and edgewise root bending moments in the clean case. (a) *TSR* = 3.0. (b) *TSR* = 4.3. (c) *TSR* = 5.6.

Appendix B: Uncertainty estimation

The experimental uncertainty of the *raw* measurement results is expressed by means of the standard deviation,

$$\sigma = \sqrt{\frac{1}{n-1}\sum_{i=1}^{n}|\mu_i - \bar{\mu}|^2}, \tag{12}$$

where n is the number of samples and $\bar{\mu}$ refers to the average result. The values of σ are rounded up conservatively and thus representative for both tripped and clean baseline cases as well as the GF configurations.

Table 2. Standard deviation and mean results of tripped baseline as reference value.

Section	Quantity	***TSR*** **= 3.0**	***TSR*** **= 4.3**	***TSR*** **= 5.6**
3.1	σ (u_∞) [ms^{-1}]	0.02 (6.57)	0.02 (6.57)	0.01 (5.02)
	σ (u) [ms^{-1}]	0.20 (4.87)	0.06 (4.55)	0.04 (3.49)
	σ (w) [ms^{-1}]	0.20 (1.06)	0.06 (1.12)	0.03 (0.71)
3.2[(a)]	σ_{min} (Δp) [Pa]	2.8 (21.8)	2.6 (102.5)	1.7 (6.1)
	σ_{max} (Δp) [Pa]	30.0 (-193.6)	5.8 (-269.1)	3.2 (-41.6)
3.3	σ (M_{flap}) [Nm]	1.9 (36.6)	2.9 (56.5)	2.2 (42.9)
	σ (M_{edge}) [Nm]	1.0 (8.5)	1.1 (9.1)	0.6 (4.4)

[(a)] Minimum and maximum standard deviation of pressure taps

As expected, the scatter of both the velocity and the pressure data depends on the OP, i.e. it is higher at stall (TSR = 3.0), see Table 2. Looking at the RBMs, however, the experimental uncertainty of σ (M_{flap}) and σ (M_{edge}) is influenced by the structural impact of the rotational frequency that the SGs register simultaneously to the aerodynamic forces. Overall, the standard deviation is not significantly influenced by either of the GF configurations.

Subsequently, the 95% confidence interval or so-called random error is computed with

$$\varepsilon = t \cdot \frac{\sigma}{\sqrt{n}} \approx 1.96 \cdot \frac{\sigma}{\sqrt{n}}, \qquad (13)$$

where t is the Student's t-distribution (Barlow, 1999).

Table 3. 95% confidence interval and mean results of tripped baseline as reference value.

Section	Quantity	***TSR*** **= 3.0**	***TSR*** **= 4.3**	***TSR*** **= 5.6**
3.1	ε (u_∞) [ms^{-1}]	$5.0\cdot10^{-5}$ (6.57)	$5.0\cdot10^{-5}$ (6.57)	$2.8\cdot10^{-5}$ (5.02)
	ε (u) [ms^{-1}]	$6.1\cdot10^{-3}$ (4.87)	$2.1\cdot10^{-3}$ (4.55)	$1.2\cdot10^{-3}$ (3.49)
	ε (w) [ms^{-1}]	$7.1\cdot10^{-3}$ (1.06)	$1.8\cdot10^{-3}$ (1.12)	$1.1\cdot10^{-3}$ (0.71)
3.2[(a)]	ε_{min} (Δp) [Pa]	$4.3\cdot10^{-2}$ (21.8)	$4.0\cdot10^{-2}$ (102.5)	$2.7\cdot10^{-2}$ (6.1)
	ε_{max} (Δp) [Pa]	$5.1\cdot10^{-1}$ (-193.6)	$8.8\cdot10^{-2}$ (-269.1)	$4.8\cdot10^{-2}$ (-41.6)
3.3	ε (M_{flap}) [Nm]	$2.9\cdot10^{-2}$ (36.6)	$4.5\cdot10^{-2}$ (56.5)	$3.4\cdot10^{-2}$ (42.9)
	ε (M_{edge}) [Nm]	$1.5\cdot10^{-2}$ (8.5)	$1.6\cdot10^{-2}$ (9.1)	$9.6\cdot10^{-3}$ (4.4)

(a) Minimum and maximum confidence interval of pressure taps

The values of the 95% confidence interval, see Table 3, are significantly smaller compared to those of the standard deviation (Table 2). The reason is the relatively large number of samples, i.e. $n \approx 3.6 \cdot 10^3$ in terms of the wake velocities, u and w, and $n \approx 1.7 \cdot 10^4$ per azimuthal angle in the remaining cases. Hence, the presented average results are contained by a reasonably small confidence interval.

Data availability.

Measurement data and results can be provided by contacting the corresponding author.

Author contribution

Jörg Alber performed the wind tunnel experiments together with Rodrigo Soto-Valle and the support of all co-authors. Jörg Alber processed the data and prepared the manuscript with the support of Marinos Manolesos and Rodrigo Soto-Valle both of whom contributed with important comments and suggestions to all section of the manuscript.

Competing interests

The authors declare that they have no conflict of interest.

Acknowledgements

The authors would like to acknowledge the constant support of the BeRT project by the researches and the technicians of the Hermann-Föttinger Institut at the Technische Universität Berlin. The authors would also like to acknowledge the technical support of SMART BLADE ®.

References

Alber, J., Pechlivanoglou, G., Paschereit, C. O., Twele, J. and Weinzierl, G.: Parametric Investigation of Gurney Flaps for the Use on Wind Turbine Blades, ASME Turbo Expo, https://doi.org/10.1115/GT2017-64475, 2017.

Bak, C., Zahle, F., Bitsche, R., Kim, T., Yde, A., Henriksen, L.C., Natarajan, A., and Hansen, M.: Description of the DTU 10 MW Reference Wind Turbine, Technical University of Denmark, DTU Wind Energy, 2013.

Barlow, J. B., Rae, W. H., Pope, A.: Low-Speed Wind Tunnel Testing, John Wiley & Sons,3rd edition, USA, https://doi.org/10.2514/2.633, 1999.

Bartholomay, S., Fruck, W. L., Pechlivanoglou, G., Nayeri, C. N. and Paschereit, C. O.: Reproducible Inflow Modifications for a Wind Tunnel Mounted Research HAWT, ASME Turbo Expo, https://doi.org/10.1115/GT2017-64364, 2017.

Bartholomay, S., Marten, D., Martínez, M. S., Alber, J., Pechlivanoglou, G., Nayeri, C. N., Paschereit, C. O., Klein, A. C., Lutz, T., and Krämer, E.: Cross-Talk Compensation for Blade Root Flap- and Edgewise Moments on an Experimental Research Wind Turbine and Comparison to Numerical Results, ASME Turbo Expo, https://doi.org/10.1115/GT2018-76977, 2018.

Bechert, D. W., Meyer, R. and Hage, W.: Drag reduction of airfoils with miniflaps - Can we learn from dragonflies?, AIAA Paper, https://doi.org/10.2514/6.2000-2315, 2000.

Burton, T., Jenkins, N., Sharpe, D. and Bossanyi, E.: Wind Energy Handbook, 2nd edition, Wiley Interscience, UK, https://doi.org/10.1002/9781119992714, 2011.

Cuerva, A., Tejero, Sanz-Andrés, A. and Navarro, J.: On multiple-path sonic anemometer measurement theory, Exp. Fluids, Bd. 34, S. 345–357, https://doi.org/10.1007/s00348-002-0565-x., 2003.

Drela, M.: XFOIL: An Analysis and Design System for Low Reynolds Number Airfoils, MIT: Massachusetts Institute of Technology, https://doi.org/10.1007/978-3-642-84010-4_1, 1989.

Fischer, J.: BWKA-1.5 TUB - Blades with Servo controlled Flaps, Smart Blade ®, Berlin, Germany, 2015.

Giguére, P., Lemayt, J. and Dumas, G.: Gurney flap effects and scaling for low-speed airfoils, AIAA Paper, https://doi.org/10.2514/6.1995-1881, 1995.

Gruschwitz, E. and Schrenk, O.: A simple method for increasing the lift of airplane wings by means of flaps, Zeitschrift fuer Fluegtechnik und Motorluftschiffahrt, Vol 23 No 20, 1933.

Hand, M., Simms, D., Fingersh, L., Jager, D., Cotrell, J., Schreck, S. and Larwood, S.: Unsteady aerodynamics experiment phase VI: wind tunnel test configurations and available data campaigns, National Renewable Energy Lab, https://doi.org/10.2172/15000240, 2001.

Hansen, M. O. L.: Aerodynamics of Wind Turbines, 2nd Edition, Earthscan, UK, https://doi.org/10.4324/9781849770408, 2015.

Herráez, I., Daniele, E. and Schepers, J. G.: Extraction of the wake induction and angle of attack on rotating wind turbine blades from PIV and CFD results, Wind Energy Science, https://doi.org/10.5194/wes-3-1-2018, 2018.

Holst, D., Pechlivanoglou, G., Kohlrausch, C. T., Nayeri, C. N. and Paschereit, C. O.: sHAWT Design: Airfoil Aerodynamics Under the Influence of Roughness, ASME Turbo Expo, https://doi.org/10.1115/GT2016-56377, 2016.

Houghton, E. L.: Aerodynamics for Engineering Students, Aerodynamics for Engineering Students, https://doi.org/10.1016/C2009-0-63882-4, 2013.

Kentfield, J.: The Influence of Free-Stream Turbulence Intensity on the Performance of Gurney-Flap Equipped Wind-Turbine Blades, Wind Engineering, https://www.jstor.org/stable/43749607, 1996.

Kheir-aldeen, M., and Hamid, A.: Experimental Study to the Effect of Gurney Flap on the Clark Y-14 Airfoil Wing Model, International Journal of Innovation and Scientific Research, ISSN 2351-8014, 2014

Klein, A. C., Bartholomay, S., Marten, D., Lutz, T., Pechlivanoglou, G., Nayeri, C. N., Paschereit, C. O., and Krämer, E.: About the suitability of different numerical methods to reproduce model wind turbine measurements in a wind tunnel with a high blockage ratio, Wind Energy Science, https://doi.org/10.5194/wes-3-439-2018, 2018.

Liebeck, R. H.: Design of subsonic airfoils for high lift, Journal of Aircraft, https://doi.org/10.2514/3.58406, 1978.

Marten, D, Wendler, J., Pechlivanoglou, G., Nayeri, C. N. and Paschereit, C. O.: Development and Application of a Simulation Tool for Vertical and Horizontal Axis Wind Turbines, ASME Turbo Expo, https://doi.org/10.1115/GT2013-94979, 2013.

Mueller-Vahl, H., Pechlivanoglou, G., Pechlivanoglou, G., Nayeri, C. N., Paschereit, C. O.: Vortex Generators for Wind Turbine Blades: A combined Wind Tunnel and Wind Turbine Parametric Study, ASME Turbo Expo, GT2012-69197, https://doi.org/10.1115/GT2012-69197, 2012.

Pechlivanoglou, G., Fuehr, S., Nayeri, C. N. and Paschereit, C. O.: The Effect of Distributed Roughness on the Power Performance of Wind Turbines, ASME Turbo Expo, https://doi.org/10.1115/GT2010-23258, 2010.

Pechlivanoglou, G., Philippidis T. P., Vey, S., Eisele, O., Nayeri, C. N. and Paschereit, C. O.: Vortex Generators for Wind Turbine Blades: Wind Tunnel Tests, Field Simulations and Structural Analysis, ASME Turbo Expo, RZGM2013-34, 2013.

Rooij, R P.J.O.M. van and Timmer, W. A.: Roughness Sensitivity Considerations for Thick Rotor Blade Airfoils, AIAA Paper 2003-0350, https://doi.org/10.2514/6.2003-350, 2003.

Schatz, M., Günther, B., and Thiele, F. Computational modeling of the unsteady wake behind Gurney-flaps, AIAA Paper, https://doi.org/10.2514/6.2004-2417, 2004.

Snel, H., Schepers, J. G., and Siccama, N. B.: Mexico project: The database and results of data processing and interpretation, AIAA Paper, https://doi.org/10.2514/6.2009-1217, 2009.

Soto-Valle, R., Bartholomay, S., Alber, J., Manolesos, M., Nayeri, C. N., Paschereit, C. O.: Determining the Angle of Attack along a Wind Turbine Rotor Blade in Wind Tunnel Experiments, Wind Energy Science, https://doi.org/10.5194/wes-2020-35, 2020.

Vestas: Lift production with Vortex Generators and Gurney Flaps, https://www.vestas.com/en/campaignsites/aerodynamicupgrades/home# (last access 01 June 2020).

Vey, S., Marten, D., Pechlivanoglou, G., Nayeri, C. and Paschereit, C. O.: Experimental and Numerical Investigations of a Small Research Wind Turbine, AIAA Paper, https://doi.org/10.2514/6.2015-3392, 2015.

Weber, F.I., Durgin, W. W. and Iohari, H.: Circulation measurements about a rapidly pitching airfoil using an ultrasonic system, AIAA Paper, https://doi.org/10.2514/6.1995-2269, 1995.

Wilcox, B. J., White, E. B. and Maniaci, D. C.: Roughness Sensitivity Comparisons of Wind Turbine Blade Sections, Sandia Report, SAND2017-11288, https://doi.org/10.2172/1404826, 2017.

Zhang, Y., van Zuijlen, A. and van Bussel, G.: The MEXICO rotor aerodynamic loads prediction: ZigZag tape effects and laminar-turbulent transition modeling in CFD, Journal of Wind Engineering and Industrial Aerodynamics, https://doi.org/10.1016/j.jweia.2017.06.002, 2017.